Transitioning to the ultimate regime of convection in three-dimensional direct numerical simulations

Nathan Carbonneau, Julien Salort, Yann Fraigneau, Didier Lucor, Francesca Chillà, Anne Sergent

Transitioning to the ultimate regime of convection in three-dimensional direct numerical simulations

Nathan Carbonneau[1,2], Julien Salort[3], Yann Fraigneau[1], Didier Lucor[1], Francesca Chillà[3] and Anne Sergent[1,4]

[1]Université Paris-Saclay, CNRS, LISN, F-91400, Orsay, France

[2]Sorbonne Université, Collège Doctoral, F-75005 Paris, France

[3]ENSL, CNRS, Laboratoire de physique, F-69342 Lyon, France

[4]Sorbonne Université, CNRS, Institut Jean Le Rond d'Alembert, F-75005 Paris, France

Corresponding author: Anne Sergent, anne.sergent@sorbonne-universite.fr

(Received xx; revised xx; accepted xx)

Turbulent convection in a rectangular cavity filled with water ($Pr = 4.4$) for a Rayleigh number ranging from $Ra = 2 \cdot 10^9$ to 10^{12} is explored numerically. The thermal boundary layer has been divided into a jet-emitting region, a jet-impacting region surrounding a shearing region, the pivotal role of which in increasing the Nusselt number is demonstrated. Using a space-local analysis, a crossover towards a transition to turbulence of the thermal and velocity boundary layers has been observed at $Ra \approx 10^{11}$, accompanied by the emergence of a plateau in the dissipation ratio (Brichet *et al.* 2025). The slight deviation of the Nusselt number from the classical Grossman-Lohse theory (Stevens *et al.* 2013) observed at $Ra = 10^{12}$ could therefore be interpreted as an initial sign of the transition to the ultimate regime.

Key words: Authors should not enter keywords on the manuscript, as these must be chosen by the author during the online submission process and will then be added during the typesetting process (see Keyword PDF for the full list). Other classifications will be added at the same time.

1. Introduction

An ideal model to study turbulent buoyancy-driven flows, which are ubiquitous in both industrial and environmental fluid flows, is the Rayleigh-Bénard (RB) convection: a fluid layer heated from below and cooled from above. In such systems, the most prevalent coherent structures are the thermal plumes and the Large Scale Circulation (LSC). The LSC consists of a descending cold jet and an ascending warm jet, connected by shearing regions along the upper and lower plates (Kadanoff 2001). Shear is reduced at the jet formation and where the jet impacts the boundary layer (BL). The former region corresponds to the jet-emitting region, and the latter to the jet-impacting region. This BL region splitting

enables to identify a shearing region, unlike the decomposition in a plume-emitting and plume-impacting region, as used for instance in Zhu *et al.* (2018); Reiter *et al.* (2021).

The flow is set by two physical parameters: the Rayleigh number Ra and the Prandtl number Pr. The main response parameters are the Nusselt number Nu, the dimensionless heat flux, and the Reynolds number Re, measuring the LSC intensity. In nature, most of the thermal-driven flows occur at very high Ra, going closer to the ultimate regime of convection where $Nu \sim Ra^{1/2}$ (Kraichnan 1962). It has been shown that a turbulent kinetic boundary-layer with a logarithmic velocity profile extending over the whole horizontal domain is not a sufficient ingredient to obtain a Nu scaling law compatible with the ultimate regime (Grossmann & Lohse 2011). In Chavanne *et al.* (1997) and Grossmann & Lohse (2011) models, a logarithmic temperature $\overline{\theta}$ profile was assumed to derive this scaling law (with different logarithmic corrections). Based on the eddy thermal diffusivity model involving a characteristic velocity leading to a logarithmic $\overline{\theta}$ profile, it is shown that the turbulent heat transport becomes the governing mechanism, see Lohse & Shishkina (2024) for a review. Mean vertical $\overline{\theta}$ profiles have been extensively observed in 2D and 3D numerical simulations (Stevens *et al.* 2011), as well as experimentally (Du Puits *et al.* 2007; Sun *et al.* 2008; Du Puits 2024). However, logarithmic $\overline{\theta}$ profiles have been observed using 2D direct numerical simulations (DNS) (Van Der Poel *et al.* 2015; Zhu *et al.* 2018; He *et al.* 2024) and, experimentally or using 3D DNS (Ahlers *et al.* 2012; Wei & Ahlers 2014), but only in the plume-emitting (or jet-emitting) region, that is close to the sidewalls if any.

Nevertheless, a logarithmic $\overline{\theta}$ profile in the jet-emitting region does not necessarily imply a change in the global heat flux scaling (He *et al.* 2024). This is probably linked to the fact that the contribution of the jet-emitting region to the global heat transport remains small compared to that of the jet-impacting region, as observed at low Ra (Blass *et al.* 2021). Using 2D DNS, Zhu *et al.* (2018) observed a steeper exponent for the scaling law of the local Nu in a plume-emitting region than in the plume-impacting region when $Ra \gtrsim 10^{13}$, with an exponent value matching the prediction for a logarithmic BL (Grossmann & Lohse 2011). Furthermore, still using 2D DNS, Reiter *et al.* (2021) found that the Nusselt number from the plume-emitting region increases with Ra until a crossover from plume-impacting-dominated to plume-emitting-dominated heat transport occurs at $Ra \sim 10^{11}$. But this question has not been addressed in 3D or experimentally.

Recently, Brichet *et al.* (2025), gathering experimental and 3D-DNS data, pointed out a universal critical Reynolds number $Re_c \approx 10^4$ beyond which dissipation is dominated by the bulk fluctuations, leading to a plateau of the dissipation ratio, called the friction coefficient (Chavanne *et al.* 1997). The nature of the flow, particularly the boundary layers, is intriguing in the context of the plateau regime. To this end, 3D DNS with $Pr = 4.4$ were performed for Ra values up to 10^{12}, that is, in our physical case, one decade above the Rayleigh number corresponding to Re_c. This article focuses specifically on thermal boundary layers, examining changes that could drive an increase in the global heat flux *via* the emergence of a logarithmic law.

The paper is organised as follows: Section 2 introduces the physical problem, the numerical setup and the global responses of the considered 3D DNS cases. Section 3 describes the BL structure, in terms of jet-emitting, shearing and jet-impacting regions based on the kinetic-energy distribution along the BL, as well as vertical profiles of temperature and horizontal velocity. Finally, Section 4 focuses on the horizontal extension of regions with a logarithmic $\overline{\theta}$ profile, showing that these regions grow with Ra, spreading into the shearing region and driving the change in the Nusselt number scaling.

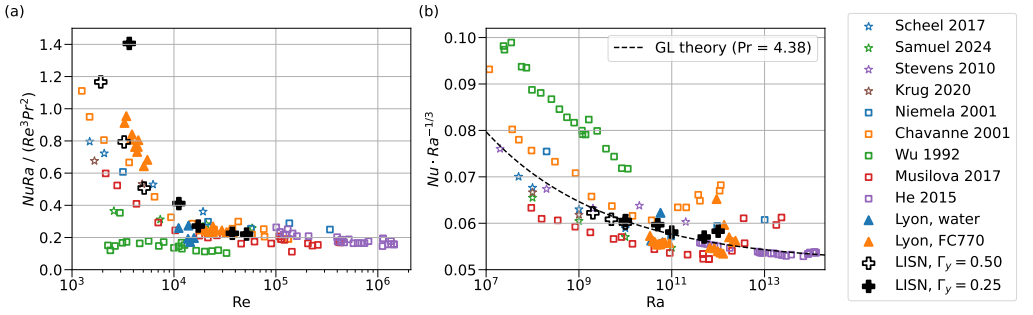

Figure 1. (a) The friction coefficient $NuRa\ /\ (Re^3Pr^2)$ plotted for Lyon's experimental data (triangles) and present 3D DNS (plus sign). 3D DNS data (stars) from Scheel & Schumacher (2017); Samuel *et al.* (2024); Stevens *et al.* (2010); Krug *et al.* (2020), and experimental data (squares) from Niemela *et al.* (2001); Chavanne *et al.* (2001); Wu & Libchaber (1992); Musilová *et al.* (2017); He *et al.* (2015) are plotted for comparison. (b) The heat transport (Nu) as a function of the Rayleigh number (Ra) for the same datasets. The displayed data points from Chavanne *et al.* (2001) are those in stringent Boussinesq conditions as defined by Roche *et al.* (2010), $2\max\left(\left|\delta A_{\text{top}}\right|/A_{\text{top}}, \left|\delta A_{\text{bottom}}\right|/A_{\text{bottom}}\right) < 20\,\%$, where $A \in \{\rho, \alpha, k, c_p, \eta\}$. The dashed line refers to the classical Grossmann-Lohse theory using the updated prefactors (Stevens *et al.* 2013).

2. Physical set-up and numerical modelling

We performed 3D DNS of RB convection in rectangular cavities of height H, with a horizontal section of width $L_x = H$ and depth $L_y = H/2$ or $H/4$, such that the cell aspect ratio $\Gamma = L_y/H = 0.5$ or 0.25, depending on the case. We employ isothermal boundary conditions on the horizontal plates, and the vertical sidewalls are adiabatic. No-slip conditions are imposed on all the boundaries. We numerically solved the dimensionless Navier-Stokes equations under the Boussinesq approximation:

$$\partial_t \mathbf{u} + \mathbf{u}\cdot\nabla\mathbf{u} = -\nabla P^* + \sqrt{Pr/Ra}\ \nabla^2\mathbf{u} + \theta\,\mathbf{e_z}, \tag{2.1}$$

$$\partial_t \theta + \mathbf{u}\cdot\nabla\theta = 1/\sqrt{Pr\,Ra}\ \nabla^2\theta \tag{2.2}$$

with $\nabla\cdot\mathbf{u} = 0$. Here t, $\mathbf{u} = (u, v, w)$, θ, P^* are dimensionless time, velocity vector, temperature and pressure, respectively. The dimensionless coordinate vector $\mathbf{x} = (x, y, z)$ is such that $\mathbf{e_z}$ is the vertical upward unit vector. The Rayleigh number is defined as $Ra = \alpha g \Delta T H^3/(\nu\kappa)$ and the Prandtl number as $Pr = \nu/\kappa$, where α is the volumetric thermal expansion coefficient, g the gravity such as $\mathbf{g} = -g\mathbf{e_z}$, ΔT is the imposed temperature difference between the horizontal plates, ν the kinematic viscosity and κ the thermal diffusivity. The Prandtl number ($Pr = 4.4$) is taken to mimic water experiment. As reference length, velocity and temperature scales, we used H, the free-fall velocity $\kappa\sqrt{RaPr}/H$ and ΔT, respectively. The temperature of the top cold plate is chosen equal to zero, so that $0 \le \theta \le 1$.

In-house second-order finite-volume solver, called SUNFLUIDH, is used to perform the simulations for $Ra \in [2\cdot10^9 - 10^{12}]$. Details and validation for the turbulent RB convection can be found in Belkadi *et al.* (2021). The mesh grid is uniform in the horizontal directions and fine enough within the BL to meet the criteria set by Shishkina *et al.* (2010).

In response to the physical parameters, a transport of heat and momentum settles inside the fluid domain that is quantified by the Nu and Re, respectively. Re is based on the peak-value of the vertical distribution of the horizontal velocity averaged in time and on the shearing region $\mathcal{S}$ (see section 3 for $\mathcal{S}$ definition). The spatial resolution has been assessed by statistical convergence of the integral heat flux, as proposed by Shishkina *et al.* (2010), with a deviation less than 1% over the simulated time interval. It can be noticed that the

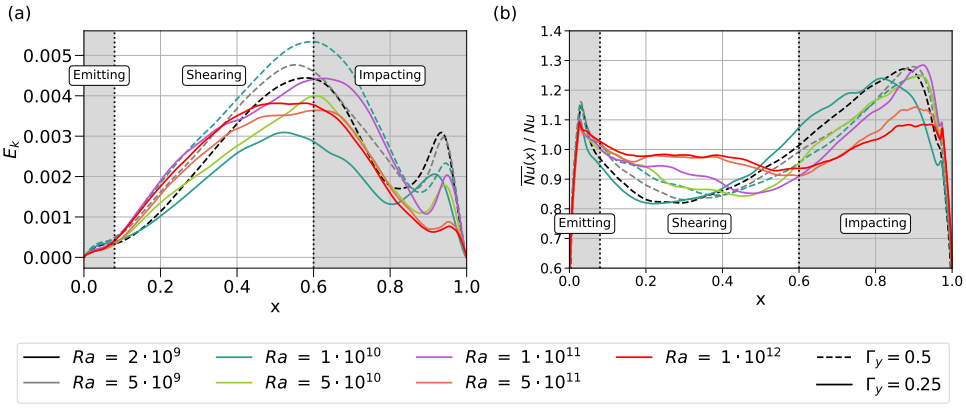

Figure 2. (a) Horizontal distribution of the kinetic energy E_k over the bottom wall computed at the top of the thermal BL ($\delta_\theta = 1/(2\,Nu)$) ; (b) The local wall Nusselt number $\overline{Nu}$ on the bottom wall normalised by the global Nusselt number Nu. All quantities are y-averaged quantities.Shaded areas correspond to jet-emitting $\mathcal{E}$ or jet-impacting $\mathcal{I}$ regions. The LSC turns clockwise, with the upward hot jet on the left and the downward cold jet on the right.

maximum grid size over the whole cavity, compared with the Kolmogorov scale (η_K), is smaller than 0.66 for all cases. To ensure that large-scale dynamics are captured, simulation times cover more than 3.5 turnover times τ (with $\tau = \pi\sqrt{Pr/Ra}\,/\,Re$). It corresponds to the time required for the LSC to perform a complete revolution in the cavity. All the simulation details and global responses are provided in the Supplementary Material.

In Brichet *et al.* (2025), our 3D DNS dataset recovers the friction coefficient plateau expressed as $NuRa/(Re^3Pr^2)$ for Re larger than $2\cdot10^4$. The figure 1.a summarises our data, as well as data from experiments and 3D DNS in the literature, illustrating the robustness of the plateau. This plateau corresponds to a regime in which the contribution to the total dissipation from the bulk becomes dominant over that of the boundary layers. The same datasets have been used in the Figure 1.b to explore the Nu scaling law. Our 3D DNS are in good agreement with the classical Grossman-Lohse (GL) theory (Stevens *et al.* 2013), except at $Ra = 10^{12}$. At this Ra value, Nu is slightly higher, hinting at a possible transition to a regime of higher heat transfer, as shown in Lyon's experiments with fluorocarbon (FC770), or in (Chavanne *et al.* 1997; Niemela *et al.* 2001; Musilová *et al.* 2017).

3. Boundary layer structure

The local BL Richardson number Ri has been used to identify the BL regions in terms of jet-emitting (referred to as $\mathcal{E}$ hereafter), wind-shearing ($\mathcal{S}$) or jet-impacting regions ($\mathcal{I}$) by Van Der Poel *et al.* (2015). Ri is based on the ratio of the potential energy E_p to the horizontal kinetic energy E_k, defined as $\langle\overline{u\,u}\rangle_y\,(x, z = \delta_\theta)$, where δ_θ is the thermal boundary layer thickness. The overline denotes the time average and $\langle\,.\,\rangle_A$ the spatial average over the direction, plane or volume called A.

However, it was difficult to determine the horizontal extent of the different BL regions from Ri distribution, particularly the $\mathcal{I}$ region, when several Ra are considered. On the contrary, a more robust definition is obtained based on E_k (see Figure 2-a), noting that the monotonic increase of E_k around the mid-width of the cavity is due to LSC shear along the horizontal plate. This is why we take (i) the slight change in slope of E_k near the wall, vertically the hot jet ($x \approx 0.08$) and (ii) the E_k maximum location ($x \approx 0.6$), as the edges of the shearing region. Variations in Ra do not appear to significantly influence these positions.

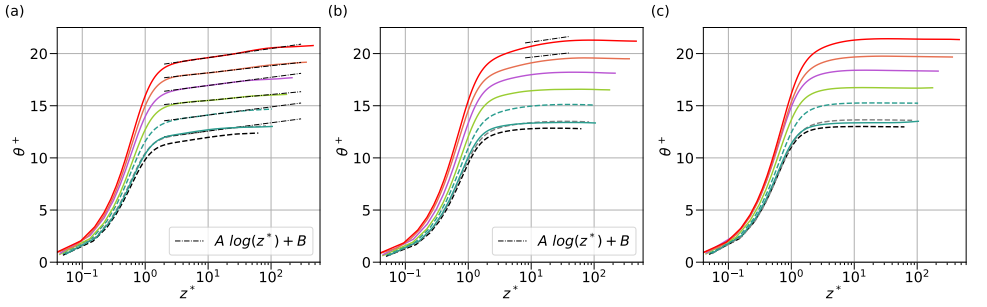

Figure 3. Mean temperature θ^+ profile (a, b, c) for different Ra (eq. 3.2), averaged on (a) the jet-emitting region, (b) the shearing region and (c) the jet-impacting region. Logarithmic fits are plotted on figure (a) for the jet-emitting regions in the ranges $Ra \geq 5 \cdot 10^9$ (or $Ra \geq 5 \cdot 10^{10}$) for $\Gamma_y = 0.5$ ($\Gamma_y = 0.25$) domains, respectively. For the two highest Ra, logarithmic fits are also plotted in figure (b) for the shearing region. Same legend for colour lines as in figure 2.

Thereby, in a first approximation, they are kept constant for all Ra, as already done by Zhu *et al.* (2018) in 2D DNS. In what follows, whatever Ra, the jet-emitting region is taken as $\mathcal{E} = (x \in [0, 0.08],\ y \in [0, \Gamma])$, the shearing region as $\mathcal{S} = (x \in [0.08, 0.6],\ y \in [0, \Gamma])$ and the jet-impacting region as $\mathcal{I} = (x \in [0.6, 1],\ y \in [0, \Gamma])$.

Despite the dispersion of the curves in Figure 2-a, two cases are clearly separate from the others in the E_k horizontal distribution: $Ra = 5 \cdot 10^{11}$ and 10^{12}. This is also the case for the distribution of the local wall Nusselt number (Figure 2-b) estimated on the bottom wall and defined as $\overline{Nu}(x) = -\left\langle \partial_z \overline{\theta} \right\rangle_y (z = 0)$. At these Ra, a quasi-plateau is noticeable for $\overline{Nu}/Nu \simeq 1$ in the $\mathcal{S}$ region, approximately localised in the BL downstream part around $x \in [0.1, 0.4]$. The $\mathcal{I}$ region is also changed with smaller values of normalised $\overline{Nu}$ and E_k, see $x \approx 0.95$. This phenomenon is consistent with the decrease of the relative contribution of the $\mathcal{I}$ region to the global heat transport observed by Reiter *et al.* (2021) in 2D DNS.

Now that the BL regions ($\mathcal{E}, \mathcal{S}, \mathcal{I}$) have been defined, it is possible to average over these regions, the BL profiles of the temperature and the streamwise velocity (Figures 3 and 4). The profiles are made dimensionless using the wall units, such as

$$z^+ = \frac{z\, u_\tau}{\sqrt{Ra/Pr}} \quad , \quad u_h^+(x,z) = \frac{\langle \overline{u_h} \rangle_y}{u_\tau} \quad , \quad u_\tau = \left(\frac{Pr}{Ra}\right)^{1/4} \sqrt{\partial_z \langle \overline{u_h} \rangle_{x \in \mathcal{S}, y}}\Big|_{z=0} \tag{3.1}$$

$$z^* = \frac{z}{\delta_\theta} \quad , \quad \theta^+(x,z) = \frac{1 - \langle \overline{\theta} \rangle_y}{T_\tau} \quad , \quad T_\tau = \frac{-1}{u_\tau \sqrt{RaPr}}\, \partial_z \langle \overline{\theta} \rangle_{x \in \mathcal{S}, y}\Big|_{z=0} \tag{3.2}$$

with u_τ the friction velocity and T_τ the friction temperature. To eliminate dependence on Ra, the temperature profiles are plotted as a function of z^*, and the velocity profiles in the flow direction are plotted as a function of z^+.

First, all the temperature θ^+ profiles display a diffusive sublayer until $z^* \approx 1$ in Figure 3, where θ^+ evolves linearly. Above, the temperature profiles reach either a constant value in the $\mathcal{S}$ and $\mathcal{I}$ regions, or present a clear logarithmic behaviour in the $\mathcal{E}$ region for $3 \lessapprox z^* \lessapprox 40$, even if it is less obvious for the cases ($Ra = 2 \cdot 10^9$; $\Gamma_y = 0.5$) or ($Ra = 10^{10}$; $\Gamma_y = 0.25$). For cases where Ra is highest, a first indication of a small logarithmic layer seems to appear in the $\mathcal{S}$ region.

Only the $\mathcal{S}$ region contains a vertical profile of horizontal velocity u_h^+ (Figure 4-a), that is representative of a boundary layer. As expected, a viscous sublayer is present in the

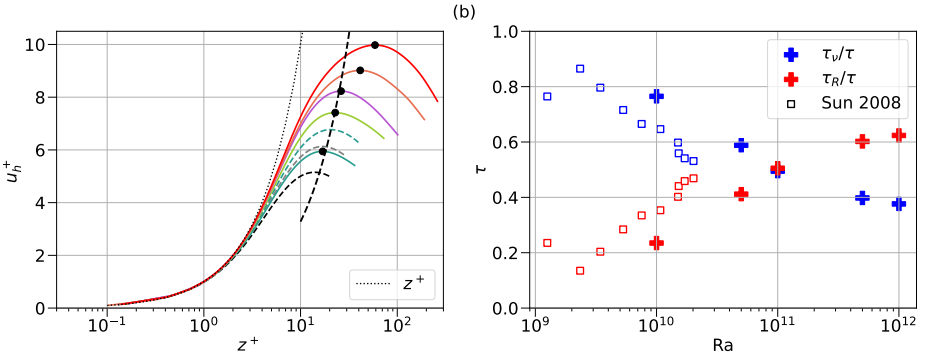

Figure 4. (a) Mean horizontal velocity u_h^+ profile for different Ra (eq. 3.1) averaged on the shearing region $\mathcal{S}$. The black circles mark the u_h^+ maximum positions, and the black dashed line is a linear curve that crosses the velocity maximum for the lowest Ra cases. Same legend for colour lines as in figure 2. (b) Viscous τ_ν (in blue) and turbulent τ_R (in red) relative contribution to the total shear stress (τ) at the viscous sub-layer height δ_ν. DNS data (filled symbols) and experimental results from Sun *et al.* (2008) (open symbols).

$\mathcal{S}$ region, where $\left\langle u_h^+ \right\rangle_{\mathcal{S}} = z^+$, but no logarithmic layer lies above it. Up to $Ra = 10^{11}$, the maximum location of u_h^+ follows a linear increase with Ra, as observed by Scheel & Schumacher (2017). For $Ra \geq 5 \cdot 10^{11}$, the boundary layer thickens more rapidly in z^+ with Ra, giving way to the possible appearance of a logarithmic law at larger Ra values. Indeed, a log layer is usually located at $z^+ \gtrapprox 50$ for a typical flat turbulent kinetic boundary layer, which is the altitude of u_h^+ maximum at $Ra = 10^{12}$. The Figure 4-b confirms that, for $Ra > 10^{11}$, the turbulent contribution (the Reynolds stress τ_R) to the shear stress becomes the predominant mechanism. It suggests that momentum transfer in the kinetic boundary layer is now also governed by turbulent fluctuations, but not yet sufficiently so to generate a significant logarithmic profile. This result is consistent with the experimental results by Sun *et al.* (2008), conducted in a rectangular convection cell filled with water, which proposed a crossover $Ra \approx 3 \cdot 10^{10}$.

4. Spatial dependence of the temperature vertical profile

Profiles in Figures 3 and 4 are averaged on $\mathcal{E}$, $\mathcal{S}$ or $\mathcal{I}$ regions. This is a classical approach. However, it is questionable, as it does not allow for observing local changes in space within the dynamics of the boundary layer, particularly in the shearing region where the first signs of a possible θ^+ logarithmic law are observed for the highest Ra. As a consequence, we propose separating the horizontal regions where the $\theta^+(z)$ profile follows a logarithmic law from the rest of the boundary layer. To do this, we retain the methodology proposed by Van Der Poel *et al.* (2015). A fit quality indicator $P(x) = A(x)/R(x)$ is introduced, that compares the amplitude A of the fit law ($\widetilde{\theta}(x, z^*) = A(x)\log(z^*) + B(x)$) to the fit residual ($R$) over the fit range (called hereafter $\mathcal{H}$). P has the advantage of distinguishing between a logarithmic profile and a constant profile, both of which yield a low R value, as a good fit of a logarithmic or linear profile provides a high or close to zero A value, respectively. Based on the figure 3.b, we test the logness of the $\theta^+(z^*)$ profile over half a decade in z^* ($\mathcal{H} = \{z^* | \, z^* \in [5, 25]\}$) whatever Ra.

Figure 5.a displays the horizontal distribution of $P(x)$ at several Ra, when the fit quality indicator is calculated at each x coordinate on the mean temperature $\theta^+(x, z^*)$ profiles (averaged over L_y). At $Ra = 10^{10}$, it is clear that any region potentially associated with a log distribution is not significant: the range of variation in P is not wide enough. But for

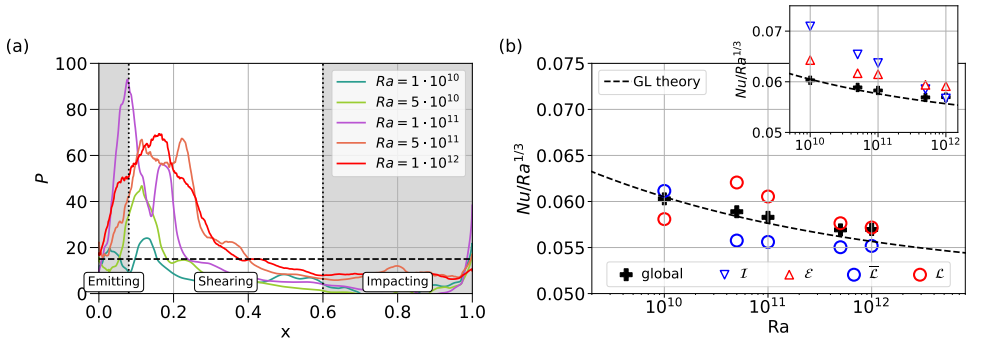

Figure 5. (a) The log quality indicator P computed for $\theta^+(x, z^*)$ profile with $z^* \in [5, 25]$ in $\Gamma_y = 0.25$ cavities. The black horizontal dashed line corresponds to the chosen threshold value $P^* = 15$. The large-scale flow moves in the direction of decreasing x coordinates. (b) Nusselt numbers as a function of Ra: the global Nusselt number Nu calculated from the present 3D DNS, Nusselt numbers averaged over two complementary regions: $\mathcal{L}$, the logarithmic region, or its complement $\overline{\mathcal{L}}$. Inset: The Nusselt number is averaged over the jet-impacting $\mathcal{I}$ or jet-emitting $\mathcal{E}$ regions.

larger Ra values, we can define the horizontal extent of the logarithmic region as the surface $\mathcal{L} = \{(x, y) \in [0, \Gamma_x] \times [0, \Gamma_y] \mid P(x, y) \geq P^*\}$, where P^* is a threshold to be chosen. It should be noted that this methodology is difficult to apply to a Ra range, as the fit range $\mathcal{H}$ is held constant for consistency. As the amplitude A increases with increasing Ra, the worst case occurs at $Ra = 10^{12}$ as a larger residual value (R) is permitted for a particular P. Here, $P^* = 15$ ensures at $Ra = 10^{12}$ a logarithmic portion of the temperature profile spanning approximately half a decade in z^* at the horizontal coordinates where $P(x, y) = P^*$. As a consequence, this threshold value appears appropriate for distinguishing the region of the logarithmic profile ($\mathcal{L}$) from the rest ($\overline{\mathcal{L}}$).

Overall, in Figure 5.a, we see that the $\mathcal{L}$ surface increases with Ra. At $Ra = 5 \cdot 10^{10}$, the logarithmic region is mainly located at the end of the shearing region. But for higher Ra, the logarithmic region extends into both the shearing and jet-emitting regions. Interestingly, for the two highest Ra, the logarithmic region is present up to approximately $x \approx 0.4$, thus encompassing the entire plateau where $\overline{Nu}/Nu \approx 1$ (see Figure 2.b), highlighting the effect of the temperature logarithmic profile on the local wall Nusselt number. This phenomenon is illustrated in the Figure 5.b, where the averaged Nusselt number over the logarithmic and non-log regions ($\mathcal{L}$ and $\overline{\mathcal{L}}$, respectively) is plotted as a function of Ra. It is shown that for $Ra \geq 5 \cdot 10^{10}$, the heat transfer occurring in $\mathcal{L}$ region is more intense than in $\overline{\mathcal{L}}$. Moreover, the global Nusselt number appears to be driven primarily by $\langle Nu \rangle_{\mathcal{L}}$ as Ra increases, $\langle Nu \rangle_{\mathcal{L}}$ and Nu getting ever closer. Besides, a comparison between the value of Nu averaged over $\mathcal{I}$ and $\mathcal{E}$ (see the inset) reveals the crossover between the Nusselt numbers from these two regions, as had already been observed in Reiter *et al.* (2021) using 2D DNS, and this for the same value of $Ra \approx 3 \cdot 10^{11}$.

However, in Figure 3, the logarithmic profile of θ^+ is only visible in $\mathcal{E}$ because the horizontal average is calculated over large areas ($\mathcal{E}$, $\mathcal{S}$ or $\mathcal{I}$), which is a rough approximation. This is confirmed by the Figure 6-a showing that the logarithmic region $\mathcal{L}$ grows in the (x, y)-plane with Ra, with a quasi-uniform $\overline{Nu}/Nu$ over a large part of the logarithmic region of $\mathcal{S}$ as already observed on the Figure 2-b. Consequently, the slight deviation of the global Nusselt number Nu from classical GL's scaling law at $Ra = 10^{12}$ (in Figure 1.b) may result not only from an increase in the local intensity of $\overline{Nu}(x, y)$, but also from an increase in the region area over which the most intense heat transfer occurs.

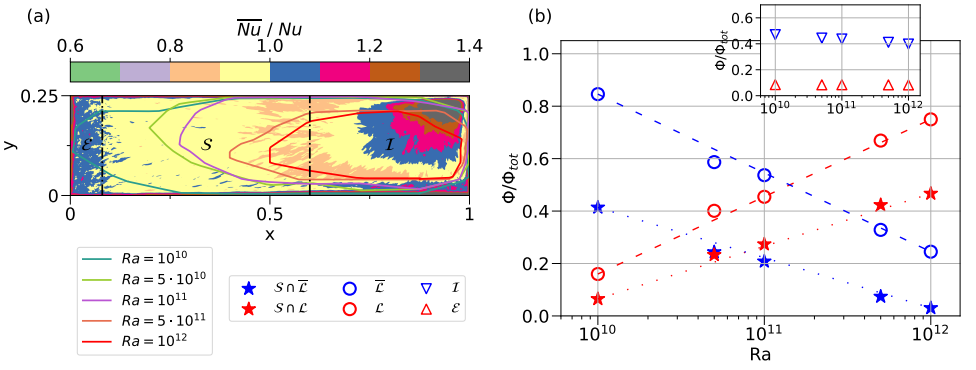

Figure 6. (a) Distribution of the normalised local Nusselt number over the bottom wall for $Ra = 5 \cdot 10^{11}$. The lines separate the logarithmic region ($\mathcal{L}$) from the non-logarithmic region ($\overline{\mathcal{L}}$) for each Ra value, according to the P^* criteria. (b) The relative contribution to the total heat flux ($\Phi_{tot} = Nu \times L_y$) of different regions. The stars correspond to the parts of the logarithmic (non-log) regions within the shearing region, denoted $\mathcal{S} \cap \mathcal{L}$ ($\mathcal{S} \cap \overline{\mathcal{L}}$, respectively).

Both effects are clearly in play when considering the relative contribution of the different regions to the global heat flux (Figure 6-b). For example, for $Ra \gtrsim 2 \cdot 10^{11}$, the relative contribution of the logarithmic region ($\Phi_{\mathcal{L}}$) to the global heat flux becomes dominant compared to $\Phi_{\overline{\mathcal{L}}}$, while their Nu are very similar in Figure 5.b. Additionally, whereas the relative contributions $\Phi_{\mathcal{I}}$ and $\Phi_{\mathcal{E}}$ remain quasi-constant ($\Phi_{\mathcal{I}}$ slightly decreases but remains four times larger than $\Phi_{\mathcal{E}}$, and $\Phi_{\mathcal{E}}$ remains marginal around 10%, see Inset), the increase of Φ_{tot} is mainly supported by the increasing contribution of the logarithmic region within $\mathcal{S}$, which has become almost entirely turbulent. A second crossover is observed at $Ra \approx 5-8 \cdot 10^{10}$, beyond which the contribution to Φ_{tot} from the logarithmic region within $\mathcal{S}$ becomes dominant compared to that from the non-logarithmic region. This suggests that the transition to turbulence in the thermal boundary layers has begun slightly earlier.

5. Conclusion

DNS of 3D turbulent RB convection have been conducted for water-filled cavities spanning almost three decades of Ra, from $Ra = 2 \cdot 10^9$ to $Ra = 10^{12}$. Two cases for $Ra > 10^{11}$ exhibit a sufficiently high LSC Reynolds number to reach a universal plateau for the quantity $NuRa/(Re^3Pr^2)$, indicating that the kinetic energy dissipation is dominated by the bulk contribution, as shown in Brichet *et al.* (2025). The case for $Ra = 10^{12}$ shows a slight deviation of the Nusselt number from the classical GL theory.

Based on these observations, the thermal BL has been examined. By taking advantage of the relationship between horizontal kinetic energy and shear, three BL regions have been robustly identified, regardless of the Ra values: the jet-emitting, shearing and jet-impacting regions. As expected from the literature, logarithmic temperature profiles have been recovered within the jet-emitting region. However, for $Ra \geq 5 \cdot 10^{11}$, a temperature profile consistent with a logarithmic law is also observed in the shearing region, but only over around a half-decade. For the same Ra range and the same region, a thickening of the velocity boundary layer is obtained, giving way to the possible appearance of a logarithmic law at larger Ra values. In this BL region, the shear stress calculated at the viscous sub-layer thickness becomes dominated by fluctuations with a crossover at $Ra = 10^{11}$, which confirms that the kinetic boundary layer is transitioning to turbulence. To track the turbulence transition of the BL, a fit quality indicator based on the log fit over a part of the

temperature profile has been calculated locally in the horizontal plane, allowing logarithmic regions to be distinguished from the rest. Contrary to the hypothesis put forward by Van Der Poel *et al.* (2015) about a jet-emitting region growing horizontally to result in a fully turbulent temperature BL, it is shown that the logarithmic region is primarily growing within the shearing region. Furthermore, a higher local Nu value has been found in the logarithmic region, highlighting the effect of the temperature logarithmic profile on the wall heat transfer. This is consistent with previous observation by Zhu *et al.* (2018) in 2D DNS of a higher Nu in the plume-emitting region, also associated with a logarithmic temperature profile. Except when $Ra = 10^{10}$, where the BLs are entirely non-turbulent, the global Nusselt number is increasingly governed by the logarithmic region. In parallel, the comparison between the Nu value averaged over the jet-emitting and jet-impacting regions reveals a crossover in terms of heat transfer efficiency at $Ra \approx 5 \cdot 10^{11}$, as had already been observed in Reiter *et al.* (2021) using 2D DNS. However, this crossover of local Nusselt numbers does not necessarily have a significant impact on the global Nusselt number, since the global Nusselt number accounts for the heat transfer surface area of each contribution. For example, the analysis of the contribution to the global heat flux from the jet-emitting region is seen as marginal, whereas that from the jet-impacting region is more significant but decreasing. The crossover between the respective contributions of the log and no-log regions is again observed for $Ra \approx 2 \cdot 10^{11}$, but the evolution of the global Nusselt number appears to be primarily due to what occurs in the shearing region from $Ra \approx 10^{11}$.

The deviation of Nu from the classical GL theory at $Ra = 10^{12}$ is very small, since this case is very close to the transition threshold. It results from thermal BLs transitioning progressively to turbulence, as does the kinetic BL. It is worth noting that the observed crossovers at $Ra \approx 10^{11}$ are consistent with the findings of 2D-DNS (Zhu *et al.* 2018; Reiter *et al.* 2021) and experimental studies (Chavanne *et al.* 1997; Sun *et al.* 2008) as well. A dissipation-ratio plateau is also present within the cavity for this Ra range. All these ingredients (BL turbulence transition, dissipation-ratio plateau) are involved in the route to the ultimate regime (Chavanne *et al.* 1997). However, the transition to the ultimate regime has been proposed to be subcritical (Roche 2020; Lohse & Shishkina 2024). As a consequence, the critical Ra around 10^{11} may be specific to our present physical configuration in terms of Prandtl number or geometry. In contrast, the supercritical mixing transition (Dimotakis 2000; Brichet *et al.* 2025) associated with the dissipation ratio plateau, corresponds to a critical Reynolds number around $2 \cdot 10^4$, placing our two test cases at the highest Ra values ($Ra \geq 5 \cdot 10^{11}$) on this universal plateau. Nevertheless, the mechanism underlying the transition to turbulence, whether related to small-scale structures of turbulence or to large-scale structures such as the LSC or intermediate BL-eddies (such as plumes, for example), as proposed by Roche (2020), remains to be determined.

Funding. This work was funded by ANR-22-CE30-0018-01 PRC 'Thermal' project. It was provided with HPC and storage resources by GENCI at IDRIS, CINES and TGCC, thanks to the grants 2022, 2023, 2024 and 2025-2A00326 on the supercomputers Jean-Zay's CSL, Joliot Curie's ROME and Adastra's GENOA partitions.

Declaration of interests The authors report no conflict of interest.

References

Ahlers, G., Bodenschatz, E., Funfschilling, D., Grossmann, S., He, X., Lohse, D., Stevens, R.J.A.M. & Verzicco, R. 2012 Logarithmic temperature profiles in turbulent Rayleigh-Bénard convection. *Phys. Rev. Lett.* **109** (11).

Belkadi, M., Sergent, A., Fraigneau, Y. & Podvin, B. 2021 On the role of roughness valleys in turbulent Rayleigh–Bénard convection. *J. Fluid Mech.* **923**, A6.

Blass, A., Verzicco, R., Lohse, D., Stevens, R.J.A.M. & Krug, D. 2021 Flow organisation in laterally unconfined Rayleigh– Bénard turbulence. *J. Fluid Mech.* **906**, A26.

Brichet, L., Carbonneau, N., Bernard, E., Braun, R., Méthivier, L., Fraigneau, Y., Lucor, D., Chillà, F., Sergent, A. & Salort, J. 2025 Universal scaling law in turbulent Rayleigh– Bénard convection with and without roughness. *J. Fluid Mech.* **1025**, A10.

Chavanne, X., Chillà, F., Castaing, B., Hébral, B., Chabaud, B. & Chaussy, J. 1997 Observation of the ultimate regime in Rayleigh-Bénard convection. *Phys. Rev. Lett.* **79** (19), 3648–3651.

Chavanne, X., Chillà, F., Chabaud, B., Castaing, B. & Hébral, B. 2001 Turbulent Rayleigh-Bénard convection in gaseous and liquid he. *Phys. fluids* **13** (5), 1300–1320.

Dimotakis, P.E. 2000 The mixing transition in turbulent flows. *Journal of Fluid Mechanics* **409**, 69–98.

Du Puits, R. 2024 Thermal boundary layers in turbulent Rayleigh-Bénard convection with rough and smooth plates: A one-to-one comparison. *Phys. Rev. Fluids* **9** (2), 023501.

Du Puits, R., Resagk, C., Tilgner, A., Busse, F. H. & Thess, A. 2007 Structure of thermal boundary layers in turbulent Rayleigh– Bénard convection. *J. Fluid Mech.* **572**, 231–254.

Grossmann, S. & Lohse, D. 2011 Multiple scaling in the ultimate regime of thermal convection. *Physics of Fluids* **23** (4), 045108.

He, J.-C., Bao, Y. & Chen, X. 2024 Turbulent boundary layers in thermal convection at moderately high Rayleigh numbers. *Physics of Fluids* **36** (2).

He, X., van Gils, D. P. M., Bodenschatz, E. & Ahlers, G. 2015 Reynolds numbers and the elliptic approximation near the ultimate state of turbulent Rayleigh-Bénard convection. *New J. Phys.* **17**, 063028.

Kadanoff, L.P. 2001 Turbulent heat flow: Structures and scaling. *Physics Today* **54** (8), 34–39.

Kraichnan, R.H. 1962 Turbulent thermal convection at arbitrary Prandtl number. *The Physics of Fluids* **5** (11), 1374–1389.

Krug, D., Lohse, D. & Stevens, R.J.A.M. 2020 Coherence of temperature and velocity superstructures in turbulent Rayleigh– Bénard flow. *J. Fluid Mech.* **887**, A2.

Lohse, D. & Shishkina, O. 2024 Ultimate Rayleigh-Bénard turbulence. *Rev. Mod. Phys.* **96** (3), 035001.

Musilová, V., Králik, T., Mantia, M. La, Macek, M., Urban, P. & Skrbek, L. 2017 Reynolds number scaling in cryogenic turbulent Rayleigh-bénard convection in a cylindrical aspect ratio one cell. *J. Fluid Mech.* **832**, 721–744.

Niemela, J. J., Skrbek, L., Sreenivasan, K. R. & Donnelly, R. J. 2001 The wind in confined thermal convection. *Journal of Fluid Mechanics* **449**, 169–178.

Reiter, P., Shishkina, O., Lohse, D. & Krug, D. 2021 Crossover of the relative heat transport contributions of plume ejecting and impacting zones in turbulent Rayleigh-Bénard convection [(a)]. *EPL* **134** (3), 34002.

Roche, P.-E. 2020 The ultimate state of convection: a unifying picture of very high Rayleigh numbers experiments. *New Journal of Physics* **22** (7), 073056.

Roche, P.-E., Gauthier, F., Kaiser, R. & Salort, J. 2010 On the triggering of the ultimate regime of convection. *New J. Phys.* **12**, 085014.

Samuel, R.J., Bode, M., Scheel, J.D., Sreenivasan, K.R. & Schumacher, J. 2024 No sustained mean velocity in the boundary region of plane thermal convection. *J. Fluid Mech.* **996**, A49.

Scheel, J.D. & Schumacher, J. 2017 Predicting transition ranges to fully turbulent viscous boundary layers in low Prandtl number convection flows. *Phys. Rev. Fluids* **2** (12), 123501.

Shishkina, O., Stevens, R., Grossmann, S. & Lohse, D. 2010 Boundary layer structure in turbulent thermal convection and its consequences for the required numerical resolution. *New J. Phys.* **12**, 075022.

Stevens, R.J.A.M., Lohse, D. & Verzicco, R. 2011 Prandtl and Rayleigh number dependence of heat transport in high Rayleigh number thermal convection. *J. Fluid Mech.* **688**, 31–43.

Stevens, R.J.A.M., van der Poel, E.P., Grossmann, S. & Lohse, D. 2013 The unifying theory of scaling in thermal convection: the updated prefactors. *Journal of Fluid Mechanics* **730**, 295–308.

Stevens, R.J.A.M., Verzicco, R. & Lohse, D. 2010 Radial boundary layer structure and nusselt number in Rayleigh– Bénard convection. *J. Fluid Mech.* **643**, 495–507.

Sun, C., Cheung, Y.-H. & Xia, K.-Q. 2008 Experimental studies of the viscous boundary layer properties in turbulent Rayleigh– Bénard convection. *J. Fluid Mech.* **605**, 79–113.

Van Der Poel, E.P., Ostilla-Mónico, R., Verzicco, R., Grossmann, S. & Lohse, D. 2015 Logarithmic mean temperature profiles and their connection to plume emissions in turbulent Rayleigh-Bénard convection. *Phys. Rev. Lett.* **115** (15).

Wei, P. & Ahlers, G. 2014 Logarithmic temperature profiles in the bulk of turbulent Rayleigh– Bénard convection for a Prandtl number of 12.3. *J. Fluid Mech.* **758**, 809–830.

Wu, W.-Z. & Libchaber, A. 1992 Scaling relations in thermal turbulence: The aspect-ratio dependence. *Phys. Rev. A* **45** (2), 842–845.

Zhu, X., Mathai, V., Stevens, R.J.A.M., Verzicco, R. & Lohse, D. 2018 Transition to the ultimate regime in two-dimensional Rayleigh-Bénard convection. *Phys. Rev. Lett.* **120** (14).

